



Graphene “bridge” in transferring hot electrons from plasmonic Ag nanocubes to TiO₂ nanosheets for enhanced visible light photocatalytic hydrogen evolution

Qingqing Lang^a, Yaohan Chen^a, Tianlong Huang^a, Lining Yang^b, Shuxian Zhong^a, Lanju Wu^a, Jianrong Chen^b, Song Bai^{a,c,*}

^a Key Laboratory of the Ministry of Education for Advanced Catalysis Materials, College of Chemistry and Life Sciences, Zhejiang Normal University, Jinhua, Zhejiang, 321004, PR China

^b College of Geography and Environmental Sciences, Zhejiang Normal University, Jinhua, Zhejiang, 321004, PR China

^c Hefei National Laboratory for Physical Sciences at the Microscale, School of Chemistry and Materials Science, University of Science and Technology of China, Hefei, Anhui, 230026, PR China

ARTICLE INFO

Keywords:

Graphene
Plasmonics
Semiconductor
Photocatalysis
Hydrogen evolution

ABSTRACT

The integration of plasmonic metal with wide-bandgap semiconductor is a promising approach to utilize the visible light without compromise of the redox ability of photogenerated charge carriers. However, a larger work function of metal than that of semiconductor is indispensable to enable the injection of hot electrons from plasmonic metal to semiconductor. In this paper, we demonstrated that reduced graphene oxide (rGO) nanosheets as conductive “bridge” can breakthrough the restriction and transfer hot electrons from Ag of smaller work function to TiO₂ of larger work function. In the design, both of the Ag nanocubes and TiO₂ nanosheets are co-deposited on the surface of rGO nanosheets to form Ag-rGO-TiO₂ structure, which was characterized by XRD, TEM, Raman and XPS spectra. On one hand, the Ag-rGO interface facilitates the transfer of hot electrons from Ag to rGO through conductor–conductor contact. On the other hand, the new formed Schottky junction on the rGO-TiO₂ interface further pumps the transferred electrons to the surface of TiO₂ for photocatalytic reduction reaction resulted from the larger work function of rGO than that of TiO₂. Enabled by this unique design, the hydrogen production activity achieved under visible light irradiation is dramatically enhanced in comparison with that of Ag-TiO₂ counterpart with the direct contact between the same Ag nanocubes and TiO₂ nanosheets. This work represents a step toward the rational interfacial design of plasmonic metal-semiconductor hybrid structures for broad-spectrum photocatalysis.

1. Introduction

Semiconductor based solar photocatalysis for chemical fuel production, such as production of H₂ from water splitting and reduction of CO₂ to hydrocarbons is an attractive and challenging approach to addressing global energy and environment issues [1–4]. The key to achieving high solar-to-chemical energy conversion efficiency is to develop high-efficient photocatalysts, which can absorb high proportion of solar photons, create high-energy electron-hole pairs, and efficiently transfer them to the surface for redox reactions [5–7]. Generally, both the light absorption ability of photocatalysts and redox ability of photogenerated carriers are greatly determined by the bandgap of the light-harvesting semiconductor (namely, the energy range between

conduction band minimum (CBM, E_c) and valence band maximum (VBM, E_v) [8,9]. In terms of redox ability of charge carriers, wide-bandgap semiconductors with more negative CBM and more positive VBM can offer higher energetic electrons and holes for reduction and oxidation half reactions in comparison with narrow-bandgap ones. However, semiconductors with wide bandgaps can only absorb UV light (wavelength (λ) < 420 nm), which accounts for a very small fraction (≈5%) of solar spectrum. While narrow-bandgap semiconductors can utilize photons from visible light (420 < λ < 780 nm, ≈43%) or near-infrared (NIR) light (780 < λ < 2500 nm, ≈52%) region, but the less negative CBM and positive VBM reduce the redox abilities of charge carriers.

To resolve the contradictions between the light absorption and

* Corresponding author at: Key Laboratory of the Ministry of Education for Advanced Catalysis Materials, College of Chemistry and Life Sciences, Zhejiang Normal University, Jinhua, Zhejiang, 321004, PR China.

E-mail address: songbai@zjnu.edu.cn (S. Bai).

<http://dx.doi.org/10.1016/j.apcatb.2017.08.045>

Received 20 March 2017; Received in revised form 21 June 2017; Accepted 14 August 2017

Available online 20 August 2017

0926-3373/ © 2017 Elsevier B.V. All rights reserved.

redox ability of photogenerated charges, the wide-bandgap semiconductors are integrated with plasmonic metal nanostructures to form hybrid photocatalysts [8,10–16]. When the incident photons are absorbed by the free electrons of plasmonic metal, the electrons will leap over the Fermi level to a higher energy level. And the formed energetic hot electrons then inject into the conduction band (CB) of semiconductor in driving the photocatalytic reduction reaction [17,18]. On one hand, metal (e.g. Au, Ag and Cu) with plasmonic band in visible or NIR region can offer complementary light absorption to wide-bandgap semiconductors as long as the photon energy meets $h\nu \geq E_{c0} - E_f$ (which has a much smaller value than $E_c - E_v$; E_{c0} is the flat-band CB potential of the semiconductor, and E_f is the Fermi level of metal). On the other hand, the CBM of the wide-bandgap semiconductor maintain relatively high-energy level, which guarantees the high reduction ability of the injected hot electrons for photocatalytic reactions.

However, not the combination of every semiconductor and plasmonic metal can realize the effective hot electron injection for photocatalytic reactions. Generally, only when the work function of semiconductor (W_s) is smaller than that of metal (W_m) ($W_m > W_s$), can the Schottky barrier be formed between the metal and semiconductor, which can suppress the backflow of injected electrons from semiconductor to metal, making sure the transfer of electrons to the semiconductor surface for reduction reaction [19–21]. In the case of $W_m < W_s$, the Schottky barrier cannot be formed so that the injected hot electrons flow back to metal, reducing the efficacy of plasmonic effect [8]. This restriction makes some plasmonic metal can not function efficiently in some plasmonic metal-semiconductor photocatalytic systems due to the relatively small W_m (such as Ag and Cu) [22].

Graphene, a unique two-dimensional carbon structure, is considered as an ideal electron-transfer medium in photocatalysis mainly due to its various advantages including superior electron mobility, large surface area, excellent optical transparency, and low cost [23–26]. For instance, Amal et al. demonstrated that graphene could be used as a solid electron mediator for a Z-scheme photocatalytic water splitting system using BiVO_4 and $\text{Ru/SrTiO}_3\text{:Rh}$ as the O_2 and H_2 photocatalysts, respectively [27]. Yu et al. used graphene as an electron bridge between TiO_2 semiconductor and MoS_2 cocatalyst for photocatalytic H_2 evolution [28]. In this work, for the first time, we demonstrate that graphene nanosheets can breakthrough the limitation and act as “bridge” to transfer hot electrons from smaller work function plasmonic metal to semiconductor of larger work function for photocatalytic applications. In the design, TiO_2 nanosheets and Ag nanocubes are co-deposited on the reduced graphene oxide (rGO) nanosheets to form a ternary Ag-rGO- TiO_2 hybrid structure. It was found that the rGO nanosheets as conductive channels can successfully conduct the hot electron flow from Ag nanocubes to TiO_2 nanosheets. As a result, the photocatalytic performance is significantly improved by the rGO nanosheets in comparison with binary Ag- TiO_2 structure with Ag nanocubes directly deposited on the TiO_2 nanosheets.

2. Experimental

2.1. Chemicals

Poly(vinyl pyrrolidone) (PVP, M.W. \approx 55000, Aldrich, 856568), NaSH (Sigma-Aldrich, 161527), ethylene glycol (EG, Sigma-Aldrich, 324558), natural graphite flake (\sim 325 mesh, Alfa Aesar), and silver trifluoroacetate (Aladdin, S109509) were used in our synthesis. All other chemicals were of analytical grade and purchased from Sinopharm Chemical Reagent Co., Ltd. The water used in all experiments was de-ionized. All chemicals were used as received without further purification.

2.2. Synthesis of TiO_2 nanosheets

The TiO_2 nanosheets were synthesized with hydrofluoric acid as a

capping agent, by modifying a method in literature [29]. In a typical synthesis, 10-mL of tetrabutyl titanate was added into a 50-mL dried Teflon autoclave. Then with vigorous magnetic stirring, 2.5 mL of hydrofluoric acid was added and the stirring was allowed to proceed for 5 min. Then the Teflon-lined stainless steel autoclave was heated at 200 °C for 24 h. After the autoclave had cooled down to room temperature, the resultant product was separated by centrifugation, and washed with water for several times. The final product was then dried at 45 °C for 12 h. Caution! Hydrofluoric acid is extremely corrosive and toxic, and should be handled with extreme care.

2.3. Synthesis of Ag nanocubes

In a typical synthesis [30], 10-mL EG was added into a 50-mL three-neck flask and pre-heated under magnetic stirring at 150 °C. 0.12-mL NaSH (3 mM in EG) was quickly injected into the heated solution. After 2 min, 1-mL HCl solution (4 mM in EG) was introduced into the reaction solution, followed by the addition of 2.5-mL PVP solution (20 mg/mL in EG) after another 2 min. Next, 2 min later, 0.8-mL solution of silver trifluoroacetate (282 mM in EG) was added. The reaction was allowed to proceed at 150 °C for 40 min. The product was collected by centrifugation, and washed with acetone and water several times to remove excess PVP. The as-obtained Ag nanocubes were redispersed in water for further use.

2.4. Synthesis of reduced graphene oxide

Graphite oxide was synthesized from natural graphite flake (\sim 325 mesh, Alfa Aesar) by a modified Hummers method [31]. In a typical procedure, 2.0 g of graphite powder was added into concentrated H_2SO_4 (80 mL) in a 500-mL flask under ice bath. Under vigorous stirring, KMnO_4 (10.0 g) and NaNO_3 (4.0 g) were gradually added, while the temperature of the mixture was kept below 10 °C for 4 h. Subsequently, the reaction mixture was stirred at 35 °C for another 4 h until it became pasty green. The mixture was then diluted with water (200 mL), after which its color changed into brownish. The addition of water was performed in an ice bath to keep the temperature below 100 °C. The mixture was then stirred for 30 min, and 15 mL of 30 wt% H_2O_2 was slowly added to the mixture to reduce the residual KMnO_4 , after which the color of the mixture changed to brilliant yellow. The mixture was re-dispersed in water and then was dialyzed for one week to remove residual salts and acids. The resulted solid was centrifuged and dried at 45 °C for 12 h. In a typical synthesis of reduced graphene oxide (rGO), 30 mg of graphite oxide was dispersed in 100 mL of water to form a graphene oxide (GO) aqueous suspension with probe sonication (Scientz-IIID, China) for 1 h. Then 200 mg of PVP (K30) was added in and the mixture was stirred for 40 h at room temperature. The as-obtained suspension was pre-heated at 95 °C under magnetic stirring. Then 40 μL hydrazine hydrate and 200 μL ammonia were added to the mixture and the reaction was allowed to proceed at 95 °C for 1 h. The product was collected by centrifugation, washed with acetone several times, and re-dispersed in water for further use.

2.5. Fabrication of Ag-rGO- TiO_2 , Ag- TiO_2 , Ag-rGO and Eosin Y (EY)-rGO- TiO_2

In the synthesis of Ag-rGO- TiO_2 , 2.5 mL (2 mg mL^{-1}) rGO aqueous dispersion was diluted with 10 mL water by sonication. Subsequently, 20 mg of TiO_2 nanosheets were added into the rGO aqueous dispersion, which was further sonicated for 10 min. Then 1.2 mL (10 mg mL^{-1}) of Ag nanocubes was added into the dispersion, and the sonication was allowed to proceed for another 10 min. The as-obtained mixture was kept static for precipitation, centrifuged, and washed with water for several times, dried at 60 °C in vacuum, and further annealed at 100 °C for 2 h to increase the contact between rGO with TiO_2 and Ag. The Ag- TiO_2 and Ag-rGO were prepared under the same experimental

conditions as Ag-rGO-TiO₂ except in the absence of rGO nanosheets and TiO₂ nanosheets, respectively. EY-sensitized rGO (EY-rGO) was prepared through mixing 1 mL (3 mg mL⁻¹) of rGO suspension with 10 mg of Eosin Y in 50 mL H₂O by magnetic stirring for 24 h. The as-obtained EY-rGO was collected by centrifugation, washed with water several times, and re-dispersed in water for further use. EY-rGO-TiO₂ was synthesized with the same synthetic method as Ag-rGO-TiO₂ except in the absence of Ag nanocubes as well as the use of EY-rGO instead of rGO.

2.6. Sample characterizations

X-ray powder diffraction (XRD) patterns were recorded by using a Philips X'Pert Pro Super X-ray diffractometer with Cu-K α radiation ($\lambda = 1.54178$ Å). X-ray photoelectron spectra (XPS) were collected on an ESCALab 250 X-ray photoelectron spectrometer, using non-monochromatized Al-K α X-ray as the excitation source. Raman spectra were recorded on a JY LABRAM-HR micro-Raman spectrophotometer with a 514.5-nm excitation laser. Transmission electron microscopy (TEM) and high-resolution TEM (HRTEM) were taken on a JEOL JEM-2100F field-emission high-resolution transmission electron microscope operated at 200 kV. UV-vis-NIR diffuse reflectance data were recorded in the spectral region of 200–800 nm with a Cary-7000 Series UV-vis-NIR spectrophotometer. To measure the content of Ag and TiO₂ in the samples, the concentrations of metal elements were measured as follows: the samples were firstly treated with a mixture of concentrated HCl and HNO₃ (3:1, volume ratio) to dissolve Ag, and then the residual solids were heating treated with a mixture of concentrated H₂SO₄ and HNO₃ (5:3, volume ratio) to dissolve TiO₂. The concentrations of metal ions were then measured with a Thermo Scientific PlasmaQuad 3 inductively-coupled plasma mass spectrometry (ICP-MS). The content of rGO was determined by sample weighing prior to the dissolution of Ag and TiO₂ for ICP-MS measurements.

2.7. Photoelectrochemical measurements

3.0 mg as-synthesized products were dispersed in a mixture of 10 μ L ethanol and 10 μ L nafion, which were then uniformly spindropped onto a 1 cm \times 1 cm indium tin oxide (ITO)-coated glass by a spin coater (SC-1B, China). Subsequently, the ITO-coated glass was heated at 80 °C in a vacuum oven for 1 h. The photocurrents were measured on a CHI 660D electrochemical station (Shanghai Chenhua, China) in ambient conditions under irradiation of a 300 W Xe lamp (Solaredge 700, China). Visible light (420 < λ < 780 nm) was used as the illumination source, which was realized by using both a 420-nm cutoff filter (long-wave-pass) and a 780-nm cutoff filter (short-wave-pass). The power density of visible light was measured to be 100 mW cm⁻² with an irradiatometer (FZ-A, Photoelectric Instrument Factory, Beijing Normal University). Standard three-electrode setup was used with the ITO coated glass as photoelectrode, a Pt foil as counter electrode, and an Ag/AgCl electrode as reference electrode. The three electrodes were inserted in a quartz cell filled with 0.5 M Na₂SO₄ electrolyte. The 0.5-M Na₂SO₄ electrolyte was purged with Ar for 30 min prior to the measurement. The photoresponse of the prepared photoelectrodes (i.e., *I*-*t*) was operated by measuring the photocurrent densities under chopped light irradiation (light on/off cycles: 60 s) at a bias potential of 0 V vs. Ag/AgCl for 400 s. The electrochemical impedance spectroscopy (EIS) was carried out in the frequency range of 10⁻¹ to 10⁵ Hz with an AC voltage amplitude of 10 mV at a bias potential of 0 V vs. Ag/AgCl.

2.8. Photocatalytic H₂ evolution measurements

To investigate the photocatalytic activities of samples in H₂ production, 15 mg photocatalysts were dispersed in 50 mL of methanol/H₂O mixture (20 vol% methanol). The samples were sonicated to form a uniform suspension, followed by saturation with Ar to eliminate air.

The light-irradiation experiment was performed by using a 300 W Xe lamp. Visible light (420 < λ < 780 nm) was used as illumination source, which was realized by using both a 420-nm cutoff filter (long-wave-pass) and a 780-nm cutoff filter (short-wave-pass). The power density of visible light was measured to be 100 mW cm⁻² with an irradiatometer (FZ-A, Photoelectric Instrument Factory, Beijing Normal University). The photocatalytic reaction was typically performed for 4 h. 1 mL gas was sampled from the reactor at a given time interval (1 h) and the amount of H₂ evolved was measured by gas chromatography (GC-2014, thermal conductivity detector, Ar carrier, Shimadzu). The liquid evolved in the photocatalytic process was analyzed by a flame ionization detector using gas chromatography (GC-2010 Plus, Shimadzu). Three replicates were collected for each sample with relative error < 10%. The during test was performed in four cycles with a 4 h-photocatalytic reaction in a cycle.

3. Results and discussion

3.1. Sample synthesis and characterization

As TiO₂ is the most widely used UV-excitabile wide-bandgap semiconductor in photocatalysis, single-crystalline TiO₂ nanosheets were used as the semiconductor model in the design, which were synthesized via a hydrothermal procedure [29]. The edge length of the nanosheets is above 200 nm and the thickness is below 5 nm, thus the area percentage of the top and bottom surface on the total surface is over 95% (Fig. S1a,b). As revealed by the HRTEM images, the top and bottom faces of the TiO₂ nanosheets are covered by (001) facets (Fig. S1c,d). The large flat surface makes TiO₂ nanosheets ideal candidates to combine with other components with large contact area for interfacial charge transfer, while the low thickness not only shortens the distance of charge transfer in bulk semiconductor and reduces the possibility of electron loss, but also increases light transmission and attenuates the shielding effect on the plasmonic metals.

The second step of the design is choosing Ag nanocubes as the plasmonic metal in fabricating the hybrid photocatalysts. The Ag nanocubes with average edge length of 50.1 nm exhibit a plasmonic band in the range of 400–500 nm (suspension in yellow color, Fig. S2a-d), which is complementary to the UV response of TiO₂ nanosheets. The Ag nanocubes are also monocrystallines enclosed by six (100) faces (Fig. S2e). The cubic profile of Ag nanocrystals ensures the face-to-face contact with the nanosheet structure of TiO₂. Our first-principles calculations have shown that the Ag(100) has a work function of 4.28 eV, smaller than that of TiO₂(001) (4.89 eV), which is not favorable to the establishment of Schottky barrier [20,21]. It should be noted that work functions of metal and semiconductor are greatly dependent on their exposed facets. For Ag and TiO₂ in other shapes, it is possible that the work function of Ag nanocrystals is larger than that of TiO₂ in forming effective Schottky junction.

In the meantime, reduced graphene oxide (rGO) nanosheets were prepared through exfoliating graphite oxide into graphene oxide (GO) nanosheets (Fig. S3a,b), and then reducing them by hydrazine hydrate. The as-obtained rGO nanosheets are in wrinkles with micro-sized flat surface and nanoscale thickness (Fig. S3c). According to the XRD patterns (Fig. S3d), graphite oxide shows a strong peak centered at $2\theta = 10.2^\circ$, corresponding to its (001) reflection, which disappears in the pattern of the resulted rGO, confirming the completely exfoliation of graphite oxide [32]. Moreover, a weak and broad peak at $2\theta = 23.2^\circ$ appears in the diffraction pattern of rGO, confirming the removal of oxygen-containing groups [33,34]. While in the Raman spectra (Fig. S3e), graphite oxide displays two prominent peaks at ca. 1359 and 1601 cm⁻¹, corresponding to the well-documented D and G bands, respectively; while for rGO, the G band moves to ca. 1583 cm⁻¹, close to the value of the pristine graphite. Moreover, the intensity ratio of the D and G band (*I*_D/*I*_G) of rGO shows an enhanced value as compared with that of graphite oxide, indicating the reduction of GO to form more

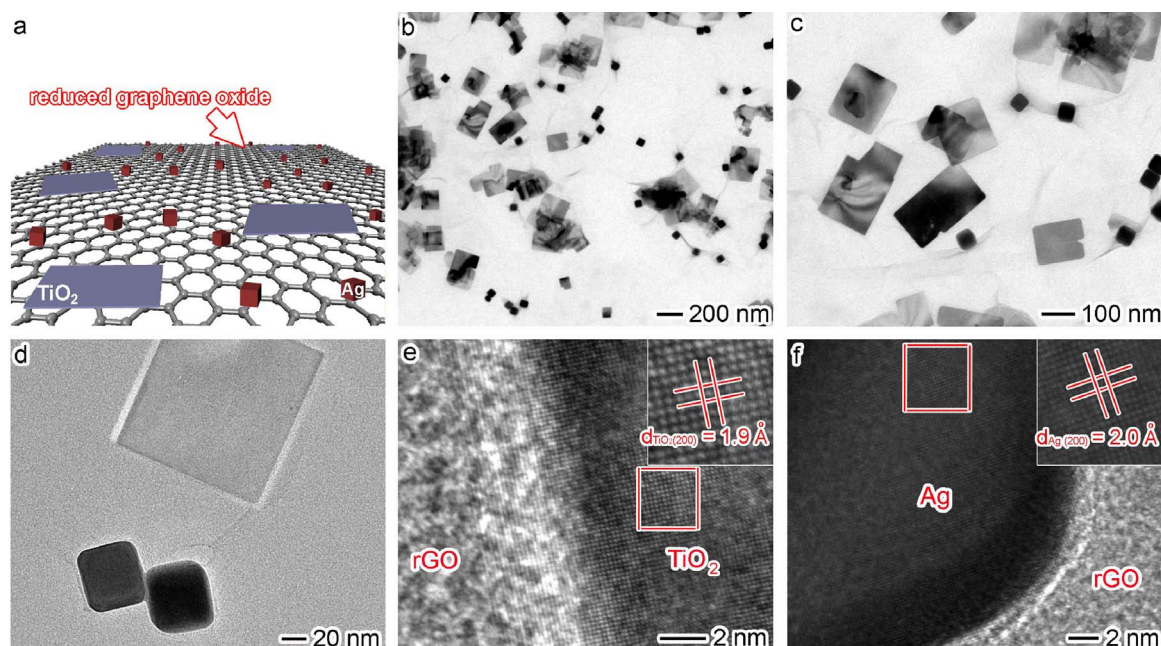


Fig. 1. (a) Schematic illustration and (b–d) TEM images of Ag-rGO-TiO₂ hybrid structure, (e,f) HRTEM images of (e) TiO₂ and (f) Ag in Ag-rGO-TiO₂ hybrid structure.

sp² domains [35].

The TiO₂ nanosheets and Ag nanocubes were then co-deposited on rGO nanosheets to form Ag-rGO-TiO₂ nanostructure through an ultrasonic self-assembly method (Fig. 1a). From the TEM images of the Ag-rGO-TiO₂ (Fig. 1b–d), it could be clearly seen that schistose TiO₂ and cubic Ag nanocrystals are uniformly distributed on the flat surface of rGO nanosheets through face-to-face contact with large interfacial area. The large interfacial area guarantees the smooth electron flow through the interfaces. The direct contact between TiO₂ and Ag can be rarely seen in the TEM images, which may be resulted from the stronger interaction between Ag and rGO as well as TiO₂ and rGO in comparison with that between Ag and TiO₂. The HRTEM images in Fig. 1e and f indicate the formation of Ag(100)-rGO and rGO-(001)TiO₂ interfaces in the Ag-rGO-TiO₂, respectively. Through measuring the content of Ag and TiO₂ with ICP-MS, the content of rGO in the Ag-rGO-TiO₂ was determined to be 12.3 wt.%.

As a reference sample of Ag-rGO-TiO₂, Ag-TiO₂ structure without rGO nanosheets was also synthesized under the same experimental conditions except in the absence of rGO precursor (Fig. 2a). As shown in Fig. 2b and c, Ag nanocubes are evenly distributed over the flat surface of TiO₂ nanosheets through facet-to-facet contact. Such direct facet-to-facet contact is better resolved by a cross-section TEM image with a standing-up TiO₂ nanosheet (Fig. S4). As a result, an Ag(100)-(001)TiO₂ interface is formed, which can be clearly seen in the HRTEM image in Fig. 2d. As confirmed by the ICP-MS, the weight ratio of Ag to TiO₂ was kept the same between Ag-rGO-TiO₂ and Ag-TiO₂ (Table S1).

The structures and phase of the as-obtained Ag-rGO-TiO₂ and Ag-TiO₂ samples were characterized by the XRD patterns (Fig. 3a) and Raman spectra (Fig. 3b) with bare TiO₂ nanosheets, Ag nanocubes and rGO nanosheets as reference samples. In the XRD pattern of bare TiO₂ nanosheets, all the diffraction peaks correspond to the anatase phase TiO₂ (JCPDS 21-1272). As for the Ag nanocubes, all the diffraction peaks can be assigned to the face-centered cubic (fcc) Ag (JCPDS 87-0597). Both the peaks of TiO₂ and Ag are shown in the XRD pattern of Ag-TiO₂, further confirming the combination of TiO₂ nanosheets and Ag nanocubes. Because of no strong peak in the XRD pattern of rGO nanosheets, the XRD pattern of Ag-rGO-TiO₂ is much similar to that of Ag-TiO₂, the only difference is the irregular baseline resulted from the weak and broad peak of rGO located at around 23°. The relative peak intensity of Ag to TiO₂ is much approximate between Ag-rGO-TiO₂ and

Ag-TiO₂, further revealing their same Ag/TiO₂ weight ratio. In the Raman spectrum of bare TiO₂ nanosheets, four Raman-active modes of E_g (140 cm⁻¹), B_{1g} (395 cm⁻¹), A_{1g} (515 cm⁻¹) and E_g (635 cm⁻¹) correspond to the anatase TiO₂ [36]. Similar peaks are also shown in the Raman spectrum of Ag-TiO₂ as a result of no obvious Raman peak of Ag nanocubes. Different from the spectrum of Ag-TiO₂, both the peaks of TiO₂ and the D and G bands of rGO are observed in the spectrum of Ag-rGO-TiO₂, further confirming the hybridization of Ag, TiO₂ and interparticulate rGO.

The composition of the as-obtained Ag-rGO-TiO₂ sample was characterized by the XPS spectra. The survey XPS spectrum indicates the Ag, C, Ti, O and N elements in the Ag-rGO-TiO₂ (Fig. S5a). In the high-resolution spectrum of Ag3d (Fig. 3c), the binding energies of 368.3 eV (Ag3d_{5/2}) and 374.3 eV (Ag3d_{3/2}) are in good agreement with the zero valence of Ag. The peaks centered at 284.5 eV and 286.7 eV in the high resolution spectrum of C1s are assigned to the C–C and C–O groups, respectively (Fig. 3d). In comparison with the C1s spectrum of graphite oxide (Fig. S6), the intensity of C–O peak in rGO decreases significantly, while the peak of C=O (288.0 eV) nearly disappears, confirming the high reduction degree of rGO through the effective removal of oxygen-containing functional groups [37]. As for the high-resolution spectrum of Ti2p (Fig. 3e), the peaks with binding energies of 459.0 eV and 464.7 eV are attributed to Ti2p_{3/2} and Ti2p_{1/2} for Ti(IV) of the titania, respectively [38,39]. The O1s peaks located at 530.0 eV and 531.6 eV are in good agreement with the O–Ti of TiO₂ and O–H of adsorbed OH groups on the TiO₂ surface, respectively (Fig. 3f). The doped N in the Ag-rGO-TiO₂ may be resulted from the rGO reduced by hydrazine hydrate [40]. The peak of N1s at 400.3 eV is in agreement with the pyrrolic N (Fig. S5b) [41].

3.2. Charge kinetics and photocatalytic performance analysis

The charge kinetics of the samples was then investigated to reveal the generation and transfer of photo-induced charge carriers during the photocatalytic process. The light absorption abilities of the samples were firstly investigated by the UV-vis-NIR diffuse reflectance spectra in Fig. 4a. Bare TiO₂ nanosheets exhibit light absorption in the UV region with absorption edge at ca. 390 eV. With the addition of Ag nanocubes to form the Ag-TiO₂, the bandgap and absorption edge of TiO₂ are not changed. And an additional peak in the range of 400–500 nm is also

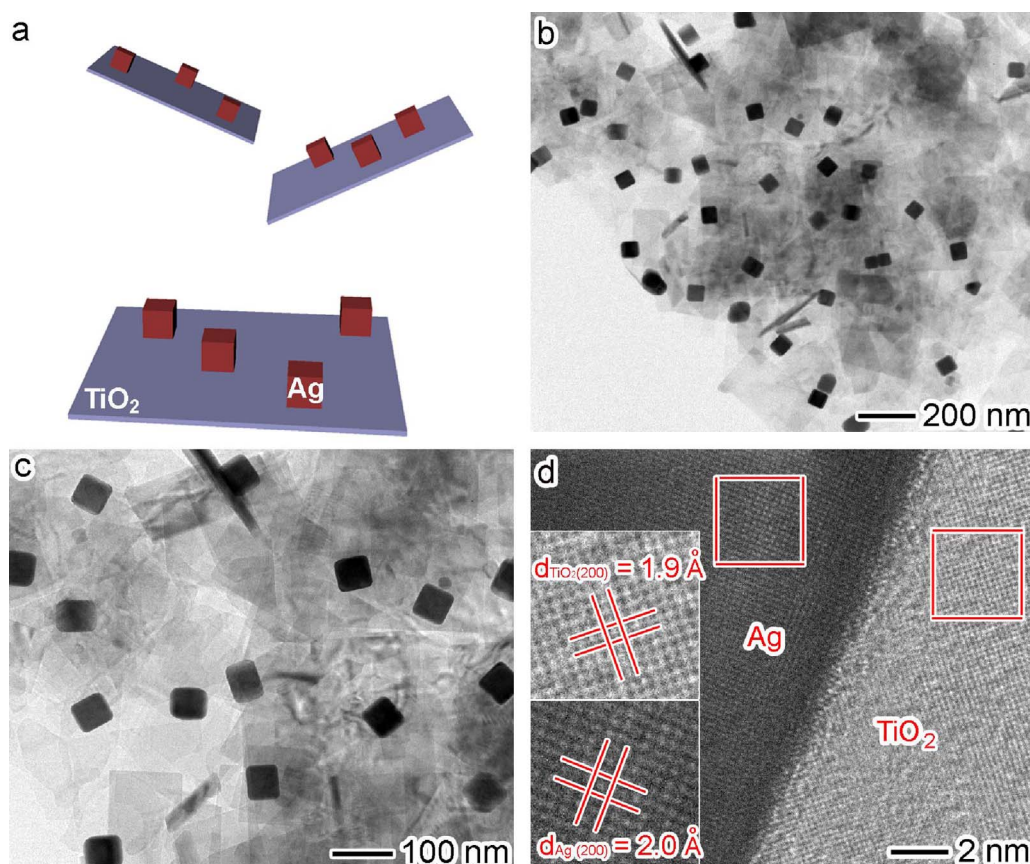


Fig. 2. (a) Schematic illustration, (b,c) TEM and (d) HRTEM images of Ag-TiO₂ hybrid structure.

observed, which is ascribed to the plasmonic absorption of Ag nanocubes (Fig. S2d). Thus the Ag nanocubes extend the light absorption of Ag-TiO₂ to visible region. In addition, as bare rGO nanosheets only have a weak light absorption throughout the UV/visible region (Fig. S7) [42], the UV-vis-NIR spectrum of Ag-rGO-TiO₂ is almost identical to that of Ag-TiO₂, confirming the comparable visible light absorption ability between them.

With the comparable visible light absorption, the plasmonic effect of Ag nanocubes on TiO₂ nanosheets was further revealed by the photoelectrochemical measurements under visible light irradiation ($420 < \lambda < 780$ nm). As shown in Fig. 4b, the photocurrent response of bare TiO₂ nanosheets is much weak, as they do not absorb photons in the visible region. Also, as compared with that of bare TiO₂, there is no obvious increase in the photocurrent response of Ag-TiO₂ though the distinct visible light absorption between them, implying that the plasmonic hot electrons generated in the visible light-excited Ag nanocubes can not effectively inject into the CB of TiO₂ nanosheets. In contrast to Ag-TiO₂, a distinctive larger photocurrent response has been observed for Ag-rGO-TiO₂, showing the occurrence of apparent charge transfer between the components. This argument is further supported by the EIS (Fig. 4c), in which the Ag-rGO-TiO₂ shows a much smaller arc radius as compared with Ag-TiO₂ and bare TiO₂ samples, confirming the superior electron transmission capability in the Ag-rGO-TiO₂.

Have confirmed the charge kinetics of the samples, their photocatalytic performance in H₂ production via water splitting was further investigated under visible light irradiation with methanol as a hole sacrificial agent. As shown in Fig. 5a, bare TiO₂ nanosheets show no photocatalytic activity in H₂ production under visible light irradiation because TiO₂ nanosheets are not visible light excitable. Also, no H₂ is produced by Ag-TiO₂, revealing that the plasmonic effect of Ag is out of work in the sample. In sharp contrast to bare TiO₂ and Ag-TiO₂, the Ag-rGO-TiO₂ sample exhibits apparent photocatalytic activity in H₂ evolution (also in Fig. S8), identifying the plasmonic hot electrons

produced by Ag nanocubes can inject into TiO₂ and participate in the reduction of H₂O to H₂ efficiently. It should be noted that no other gaseous or liquid reduction product was detected during the photocatalytic process. The as-obtained Ag-rGO-TiO₂ sample also exhibits excellent photocatalytic stability. After four photocatalytic cycles, Ag nanocubes and TiO₂ nanosheets are well retained on the rGO substrate without any change in the shapes (Fig. S9), confirming the intimate contact between rGO with Ag and TiO₂ components. As a result, there is only a slight decline in the average H₂ production rate during the successive cycles (Fig. 5b and Fig. S10).

3.3. Photocatalytic mechanism analysis

To further analyze the photocatalytic mechanism of the above experimental results, the architectural structures of the Ag-TiO₂ and Ag-rGO-TiO₂ are firstly taken into consideration. The Ag-TiO₂ and Ag-rGO-TiO₂ structures possess the same Ag nanocubes for light absorption as well as the same TiO₂ nanosheets for surface reduction reaction, guaranteeing the comparable light absorption ability in hot electron generation as well as the equivalent surface adsorption and activation abilities of reactants in electron consumption. The only difference between Ag-TiO₂ and Ag-rGO-TiO₂ is the interface between Ag nanocubes and TiO₂ nanosheets, which greatly determines the electron transfer capability. In the sample of Ag-TiO₂, the direct contact between the two components results in the formation of Ag(100)-(001)TiO₂ interface, while in Ag-rGO-TiO₂ structure, both Ag(100)-rGO and rGO-(001)TiO₂ interfaces are formed with rGO nanosheets as the intermediate bridge. Based on the experimental results, the synergism of Ag(100)-rGO and rGO-(001)TiO₂ interfaces rather than Ag(100)-(001)TiO₂ interface can offer a smooth hot electron transfer path.

The first-principles calculations by us have shown that the work function of Ag(100) and TiO₂(001) are 4.28 eV and 4.89 eV, respectively (Fig. S11) [21]. While the work function of rGO was found to be

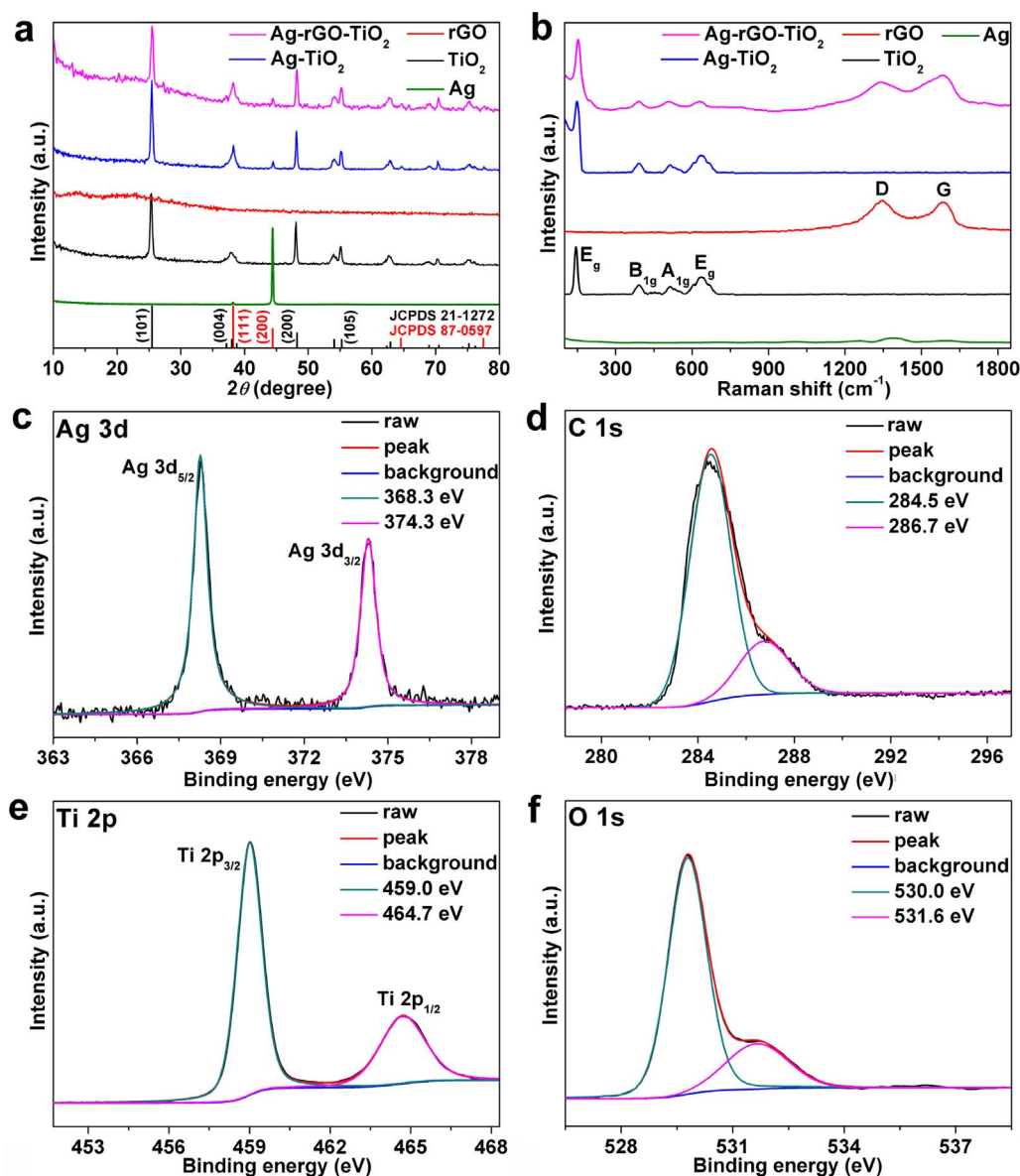


Fig. 3. (a) XRD patterns and (b) Raman spectra of bare TiO₂ nanosheets, Ag nanocubes, rGO nanosheets, Ag-TiO₂ and Ag-rGO-TiO₂ hybrid structures; (c-f) XPS spectra of Ag-rGO-TiO₂ hybrid structure: (c) Ag 3d; (d) C 1s; (e) Ti 2p and (f) O 1s high-resolution spectra.

tunable between 5.0 eV and 5.5 eV, in which the 0.5 eV variation within this range is allowed by adjusting the reduction conditions [43]. Thus the work functions of Ag(100) and TiO₂(001) can not meet the criteria for establishing the Schottky contact between metal and semiconductor, making the hot electron injection from Ag into TiO₂ is of no avail in the Ag-TiO₂ sample. As shown in Fig. 6a, no Schottky barrier is formed between Ag and TiO₂, and the injected hot electrons in TiO₂ will flow back to Ag and recombine with hot holes. While in the designed Ag-rGO-TiO₂ sample, as for the Ag(100)-rGO interface, considering both Ag and rGO are conductive materials, no barrier is necessary to facilitate the electron transfer between them. The hot electrons generated in Ag nanocubes of smaller work function flow to rGO of larger work function through a conductor-conductor contact so as to equilibrate the electron Fermi distribution at their interface [44,45]. Then the rGO nanosheets act as the conductive channel can further transmit the electrons to the rGO-TiO₂ interface. In the rGO-TiO₂ interface, as the work function of rGO is larger than that of TiO₂(001), a Schottky junction can be formed between rGO and TiO₂ [46,47]. Owing to the light absorption of rGO in visible region, the transferred electrons in rGO nanosheets can be further injected to the CB of TiO₂ under visible light excitation. As the formed rGO-TiO₂ Schottky barrier could prevent

the backflow of the injected electrons, H₂O molecules are reduced into H₂ by the injected electrons on the surface of TiO₂. The proposed photocatalytic mechanism of Ag-rGO-TiO₂ is illustrated in Fig. 6b.

To further confirming the proposed photocatalytic mechanism, the charge kinetics in the Ag-rGO and rGO-TiO₂ interfaces were investigated, respectively. For one thing, rGO nanosheets supported Ag nanocubes (Ag-rGO) was synthesized according to the same synthetic method as Ag-rGO-TiO₂ except in the absence of TiO₂ nanosheets (Fig. 7a and Fig. S12). The photoelectrochemical properties of Ag-rGO were measured in comparison with those of bare Ag nanocubes and rGO nanosheets. As shown in Fig. 7b, the photocurrent response of Ag-rGO is larger than that of Ag and rGO under visible light irradiation, revealing that the plasmonic hot electrons generated in Ag nanocubes can transfer to rGO nanosheets through the Ag-rGO interface. For another, the rGO nanosheets were firstly grafted by Eosin Y dye as visible-light sensitizer to form EY-sensitized rGO (EY-rGO). Eosin Y molecules can be easily adsorbed on the surface of rGO nanosheets through π - π stacking and esterlike linkage reaction between EY and rGO [48]. Then TiO₂ nanosheets were loaded onto the EY-rGO nanosheets to form EY-rGO-TiO₂ with the same synthetic method as Ag-rGO-TiO₂ except in the absence of Ag nanocubes as well as the use of EY-rGO instead of rGO

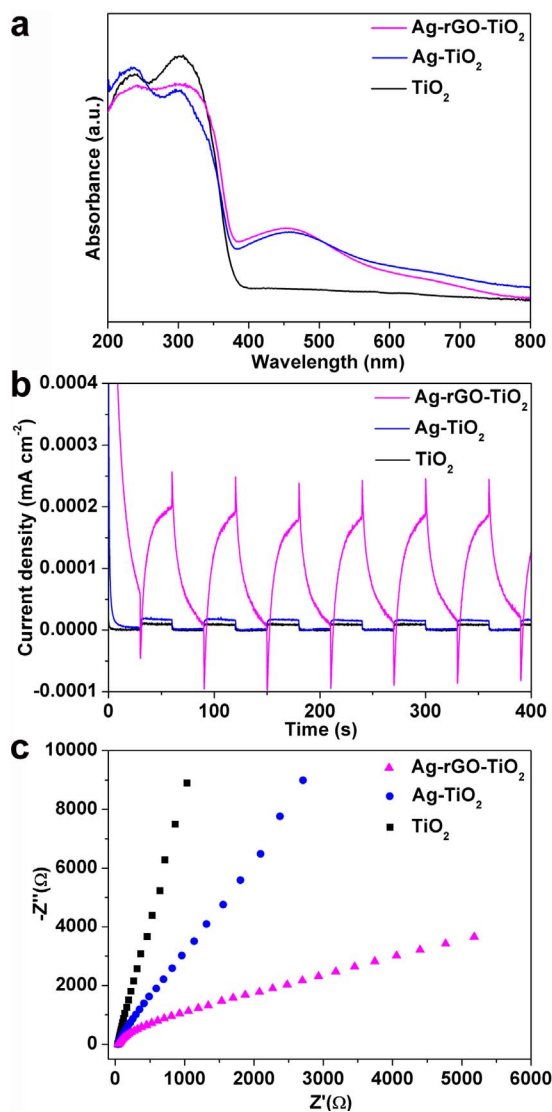


Fig. 4. (a) UV-vis-NIR diffuse reflectance spectra of bare TiO₂ nanosheets, Ag-TiO₂ and Ag-rGO-TiO₂ hybrid structures; (b) photocurrent vs. time (I-t) curves and (c) EIS Nyquist plots of bare TiO₂, Ag-TiO₂ and Ag-rGO-TiO₂ hybrid structures at 0 V vs. Ag/AgCl under visible light ($420 < \lambda < 780$ nm) irradiation.

(Fig. 7c and Fig. S13). The Eosin Y as a photosensitizer can harvest visible light, excite the electrons from the highest-occupied molecular orbital to the lowest-unoccupied molecular orbital, and transfer them to rGO nanosheets [49]. Under visible light irradiation, the as-obtained EY-rGO-TiO₂ exhibit apparent larger photocurrent in comparison with EY-rGO, confirming the rGO-TiO₂ interface can transfer the electrons

from rGO to TiO₂ successfully for photocatalytic reduction reactions [50] (Fig. 7d). The photosensitization role of EY is confirmed by the obvious photocatalytic H₂ production in EY-rGO-TiO₂ rather than rGO-TiO₂ without EY decoration (Fig. S14). It should be noted that the TiO₂ nanosheets are not photoexcited by the visible light ($\lambda > 420$ nm), thus the other two possible mechanisms for plasmonic effect (i.e., local electromagnetic field enhancement and resonant photon scattering) do not need to consider in our systems [8,51].

Furthermore, it was found that both the loading amount of Ag and the content of rGO also influence the photocatalytic activity of Ag-rGO-TiO₂, in which the average H₂ production rate has a volcano relationship with the content of Ag and rGO, respectively (Table S2). According to the proposed photocatalytic mechanism, lower loading amount of Ag decreases the light absorption ability of the photocatalyst, while higher content of rGO supporter increases the distance between Ag and TiO₂ for hot electron transfer, raising the possibility of electron loss. On the other hand, higher loading amount of Ag or lower content of rGO supporter inevitably leads to the direct contact between Ag and TiO₂ for inefficient interfacial electron transfer.

4. Conclusions

In summary, interface design was performed on plasmonic metal-semiconductor hybrid structure for enhanced visible-light photocatalytic performance with rGO nanosheets as interparticulate electron mediator. Ag-rGO-TiO₂ hybrid structure was synthesized through the deposition of Ag nanocubes and TiO₂ nanosheets onto rGO nanosheets. As a reference sample, Ag-TiO₂ structure with Ag nanocubes directly deposited on the surface of TiO₂ nanosheets was also synthesized. It was found that the hot electrons generated in plasmonic Ag can not inject into TiO₂ smoothly through the Ag-TiO₂ interface, because the work function of Ag is too small to form the Schottky barrier in preventing the backflow of the injected hot electrons. While in the Ag-rGO-TiO₂, rGO nanosheets act a “bridge” can conduct the hot electron flow from Ag to TiO₂ through the Ag-rGO and rGO-TiO₂ interfaces. The conductor-conductor contact between Ag and rGO facilitates the hot electron transfer through the Ag-rGO interface, while the Schottky barrier formed on the rGO-TiO₂ interface ensures the successful hot electrons injection from rGO into TiO₂. As a result, in contrary to Ag-TiO₂, Ag-rGO-TiO₂ exhibits obvious photocatalytic H₂ production under visible light irradiation. The present study paves a new way of using the attractive graphene materials in the interface design of high-efficient plasmonic photocatalytic systems.

Acknowledgements

This work was financially supported by National Natural Science Foundation of China (No. 21603191), Zhejiang Provincial Natural Science Foundation of China (No. LQ16B010001), Public Welfare Technology Application Research Plan Project of Zhejiang Province (Analysis Test Item, No. 2017C37024) and Project of Science and

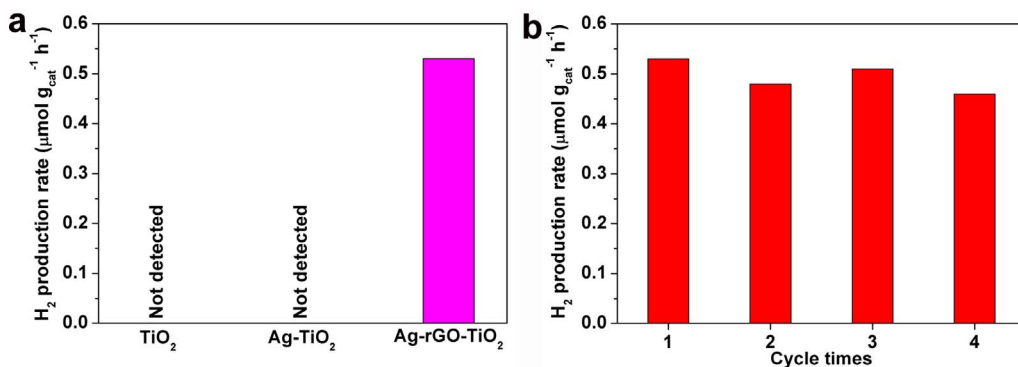


Fig. 5. (a) Photocatalytic average rates of hydrogen production under visible light ($420 < \lambda < 780$ nm) irradiation with bare TiO₂ nanosheets, Ag-TiO₂ and Ag-rGO-TiO₂ hybrid structures as catalysts; (b) photocatalytic average hydrogen production rates of Ag-rGO-TiO₂ under visible light ($420 < \lambda < 780$ nm) irradiation in four successive cycles.

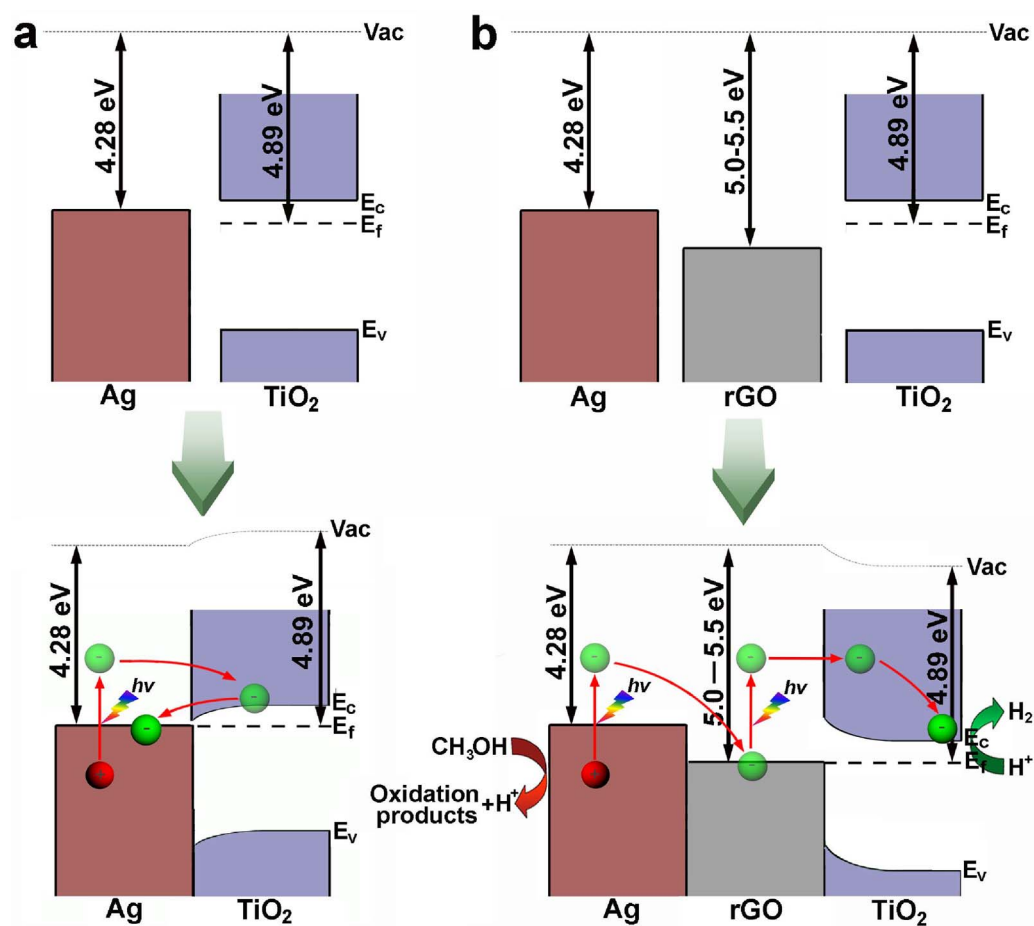


Fig. 6. Schematic illustrating the photocatalytic mechanism for the (a) Ag-TiO₂ and (b) Ag-rGO-TiO₂ samples under visible light irradiation.

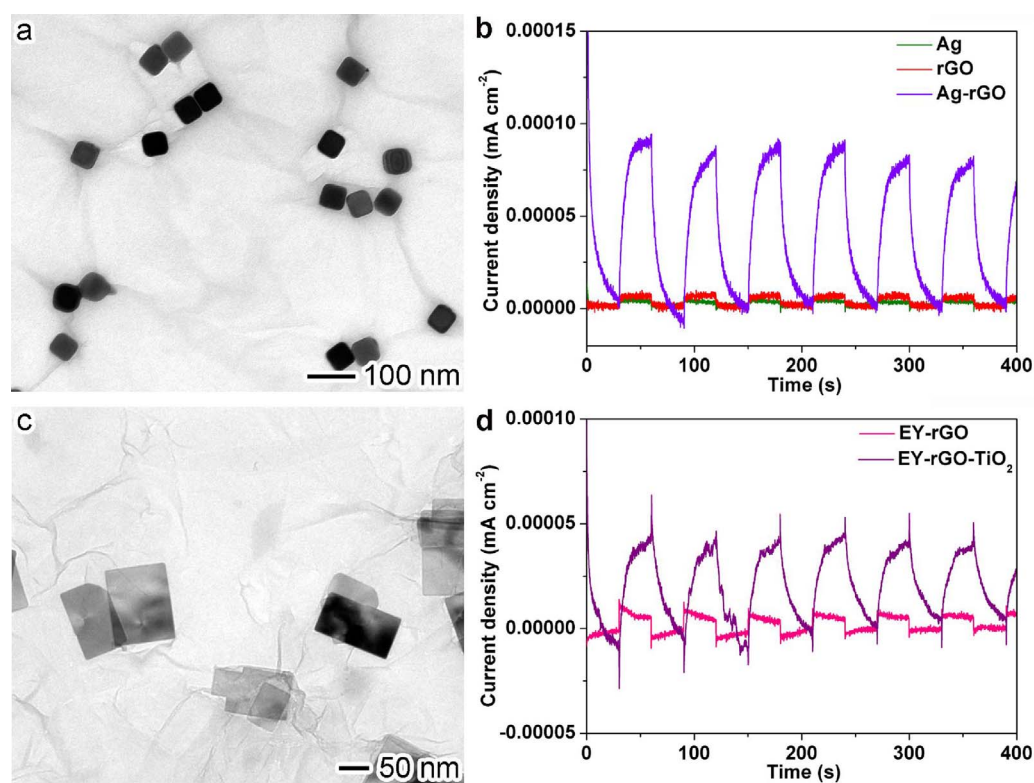


Fig. 7. (a) TEM image of Ag-rGO; (b) photocurrent vs. time (I-t) curves of Ag-rGO, bare Ag nanocubes and rGO nanosheets at 0 V vs. Ag/AgCl under visible light (420 < λ < 780 nm) irradiation; (c) TEM image of EY-rGO-TiO₂; (d) photocurrent vs. time (I-t) curves of EY-rGO-TiO₂ and EY-rGO at 0 V vs. Ag/AgCl under visible light (420 < λ < 780 nm) irradiation.

Technology Innovation Program of University Students in Zhejiang Province (No. 2017R404066).

Appendix A. Supplementary data

Supplementary data associated with this article can be found, in the online version, at <http://dx.doi.org/10.1016/j.apcatb.2017.08.045>.

References

- [1] X. Chen, S. Shen, L. Guo, S.S. Mao, Semiconductor-based photocatalytic hydrogen generation, *Chem. Rev.* 110 (2010) 6503–6570.
- [2] A. Kudo, Y. Miseki, Heterogeneous photocatalyst materials for water splitting, *Chem. Soc. Rev.* 38 (2009) 253–278.
- [3] W. Tu, Y. Zou, Z.G. Zhou, Photocatalytic conversion of CO₂ into renewable hydrocarbon fuels: state-of-the-art accomplishment, challenges, and prospects, *Adv. Mater.* 26 (2014) 4607–4626.
- [4] S.N. Habisreutinger, L. Schmidt-Mende, J.K. Stolarczyk, Photocatalytic reduction of CO₂ on TiO₂ and other semiconductors, *Angew. Chem. Int. Ed.* 52 (2013) 7372–7408.
- [5] A.L. Linsebigler, G. Lu, J.T. Yates Jr., Photocatalysis on TiO₂ surfaces: principles, mechanisms, and selected results, *Chem. Rev.* 95 (1995) 735–758.
- [6] Y. Ma, X. Wang, Y. Jia, X. Chen, H. Han, C. Li, Titanium dioxide-based nanomaterials for photocatalytic fuel generations, *Chem. Rev.* 114 (2014) 9987–10043.
- [7] A. Kubacka, M. Fernandez-Garcia, G. Colon, Advanced nanoarchitectures for solar photocatalytic applications, *Chem. Rev.* 112 (2012) 1555–1614.
- [8] S. Bai, J. Jiang, Q. Zhang, Y. Xiong, Steering charge kinetics in photocatalysis: intersection of materials syntheses, characterization techniques and theoretical simulations, *Chem. Soc. Rev.* 44 (2015) 2893–2939.
- [9] H. Tong, S. Ouyang, Y. Bi, N. Umezawa, M. Oshikiri, J. Ye, Nano-photocatalytic materials: possibilities and challenges, *Adv. Mater.* 24 (2012) 229–251.
- [10] S. Linic, P. Christopher, D.B. Ingram, Plasmonic-metal nanostructures for efficient conversion of solar to chemical energy, *Nat. Mater.* 10 (2011) 911–921.
- [11] R. Jiang, B. Li, C. Fang, J. Wang, Metal/semiconductor hybrid nanostructures for plasmon-enhanced applications, *Adv. Mater.* 26 (2014) 5274–5309.
- [12] X. Zhang, Y.L. Chen, R.S. Liu, D.P. Tsai, Plasmonic photocatalysis, *Rep. Prog. Phys.* 76 (2013) 046401.
- [13] M. Tahir, B. Tahir, N.A.S. Amin, Synergistic effect in plasmonic Au/Ag alloy NPs coated TiO₂ NWs toward visible-light enhanced CO₂ photoreduction to fuels, *Appl. Catal. B: Environ.* 180 (2016) 130–138.
- [14] K. Li, T. Peng, Z. Ying, S. Song, J. Zhang, Ag-loading on brookite TiO₂ quasi nanocubes with exposed {210} and {001} facets: activity and selectivity of CO₂ photoreduction to CO/CH₄, *Appl. Catal. B: Environ.* 204 (2017) 548–560.
- [15] M. Tahir, B. Tahir, N.A.S. Amin, Z.Y. Zakaria, Photo-induced reduction of CO₂ to CO with hydrogen over plasmonic Ag-NPs/TiO₂ NWs core/shell hetero-junction under UV and visible light, *J. CO₂ Util.* 18 (2017) 250–260.
- [16] K. Awazu, M. Fujimaki, C. Rockstuhl, J. Tominaga, H. Murakami, Y. Ohki, N. Yoshida, T. Watanabe, A plasmonic photocatalyst consisting of silver nanoparticles embedded in titanium dioxide, *J. Am. Chem. Soc.* 130 (2008) 1676–1680.
- [17] C.G. Silva, R. Juárez, T. Marino, R. Molinari, H. García, Influence of excitation wavelength (UV or visible light) on the photocatalytic activity of titania containing gold nanoparticles for the generation of hydrogen or oxygen from water, *J. Am. Chem. Soc.* 133 (2011) 595–602.
- [18] W. Ye, R. Long, H. Huang, Y. Xiong, Plasmonic nanostructures in solar energy conversion, *J. Mater. Chem. C* 5 (2017) 1008–1021.
- [19] C. Clavero, Plasmon-induced hot-electron generation at nanoparticle/metal-oxide interfaces for photovoltaic and photocatalytic devices, *Nat. Photonics* 8 (2014) 95–103.
- [20] S. Bai, X. Li, Q. Kong, R. Long, C. Wang, J. Jiang, Y. Xiong, Toward enhanced photocatalytic oxygen evolution: synergistic utilization of plasmonic effect and Schottky junction via interfacing facet selection, *Adv. Mater.* 27 (2015) 3444–3452.
- [21] W. Jiang, S. Bai, L. Wang, X. Wang, L. Yang, Y. Li, D. Liu, X. Wang, Z. Li, J. Jiang, Y. Xiong, Integration of multiple plasmonic and co-catalyst nanostructures on TiO₂ nanosheets for visible-near-infrared photocatalytic hydrogen evolution, *Small* 12 (2016) 1640–1648.
- [22] H.B. Michaelson, The work function of the elements and its periodicity, *J. Appl. Phys.* 48 (1977) 4729–4733.
- [23] Q. Xiang, J. Yu, M. Jaroniec, Graphene-based semiconductor photocatalysts, *Chem. Soc. Rev.* 41 (2012) 782–796.
- [24] S. Bai, X. Shen, Graphene-inorganic nanocomposites, *RSC Adv.* 2 (2012) 64–98.
- [25] S. Bai, Y. Xiong, Recent advances in two-dimensional nanostructures for catalysis applications, *Sci. Adv. Mater.* 7 (2015) 2168–2181.
- [26] S. Bai, J. Ge, L. Wang, M. Gong, M. Deng, Q. Kong, L. Song, J. Jiang, Q. Zhang, Y. Luo, Y. Xie, Y. Xiong, A unique semiconductor-metal-graphene stack design to harness charge flow for photocatalysis, *Adv. Mater.* 26 (2014) 5689–5695.
- [27] A. Iwase, Y.H. Ng, Y. Ishiguro, A. Kudo, R. Amal, Reduced graphene oxide as a solid-state electron mediator in Z-scheme photocatalytic water splitting under visible light, *J. Am. Chem. Soc.* 133 (2011) 11054–11057.
- [28] Q. Xiang, J. Yu, M. Jaroniec, Synergetic effect of MoS₂ and graphene as cocatalysts for enhanced photocatalytic H₂ production activity of TiO₂ nanoparticles, *J. Am. Chem. Soc.* 134 (2012) 6575–6578.
- [29] X. Han, Q. Kuang, M. Jin, Z. Xie, L. Zheng, Synthesis of titania nanosheets with a high percentage of exposed (001) facets and related photocatalytic properties, *J. Am. Chem. Soc.* 131 (2009) 3152–3153.
- [30] B. Li, R. Long, X. Zhong, Y. Bai, Z. Zhu, X. Zhang, M. Zhi, J. He, C. Wang, Z.Y. Li, Y. Xiong, Investigation of size-dependent plasmonic and catalytic properties of metallic nanocrystals enabled by size control with HCl oxidative etching, *Small* 8 (2012) 1710–1716.
- [31] W.S. Hummers, R.E. Offeman, Preparation of graphite oxide, *J. Am. Chem. Soc.* 80 (1958) 1339.
- [32] S. Bai, X. Shen, G. Zhu, A. Yuan, J. Zhang, Z. Ji, D. Qiu, The influence of wrinkling in reduced graphene oxide on their adsorption and catalytic properties, *Carbon* 60 (2013) 157–168.
- [33] H.J. Shin, K.K. Kim, A. Benayad, S.M. Yoon, H.K. Park, I.S. Jung, M.H. Jin, H.K. Jeong, J.M. Kim, J.Y. Choi, Y.H. Lee, Efficient reduction of graphite oxide by sodium borohydride and its effect on electrical conductance, *Adv. Funct. Mater.* 19 (2009) 1987–1992.
- [34] Z.J. Fan, W. Kai, J. Yan, T. Wei, L.J. Zhi, J. Feng, Y. Ren, L.P. Song, F. Wei, Facile synthesis of graphene nanosheets via Fe reduction of exfoliated graphite oxide, *ACS Nano* 5 (2011) 191–198.
- [35] S. Bai, X. Shen, G. Zhu, M. Li, H. Xi, K. Chen, In situ growth of Ni_xCo_{100-x} nanoparticles on reduced graphene oxide nanosheets and their magnetic and catalytic properties, *ACS Appl. Mater. Interfaces* 4 (2012) 2378–2386.
- [36] S. Bai, L. Wang, X. Chen, J. Du, Y. Xiong, Chemically exfoliated metallic MoS₂ nanosheets: a promising supporting co-catalyst for enhancing the photocatalytic performance of TiO₂ nanocrystals, *Nano Res.* 8 (2015) 175–183.
- [37] S. Bai, X. Shen, X. Zhong, Y. Liu, G. Zhu, X. Xu, K. Chen, One-pot solvothermal preparation of magnetic reduced graphene oxide-ferrite composites for organic dye removal, *Carbon* 50 (2012) 2337–2346.
- [38] Y. Zhu, Z. Xu, W. Jiang, S. Zhong, L. Zhao, S. Bai, Engineering on the edge of Pd nanosheet cocatalysts for enhanced photocatalytic reduction of CO₂ to fuels, *J. Mater. Chem. A* 5 (2017) 2619–2628.
- [39] Y. Zhu, Z. Xu, Q. Lang, W. Jiang, Q. Yin, S. Zhong, S. Bai, Grain boundary engineered metal nanowire cocatalysts for enhanced photocatalytic reduction of carbon dioxide, *Appl. Catal. B: Environ.* 206 (2017) 282–292.
- [40] S. Chen, J. Duan, J. Ran, M. Jaroniec, S.Z. Qiao, N-doped graphene film-confined nickel nanoparticles as a highly efficient three-dimensional oxygen evolution electrocatalyst, *Energy Environ. Sci.* 6 (2013) 3693–3699.
- [41] W. Ding, Z. Wei, S. Chen, X. Qi, T. Yang, J. Hu, D. Wang, L.J. Wan, S.F. Alvi, L. Li, Space-confinement-induced synthesis of pyridinic- and pyrrolic-nitrogen-doped graphene for the catalysis of oxygen reduction, *Angew. Chem. Int. Ed.* 52 (2013) 11755–11759.
- [42] C. Lavarato, A. Primo, R. Molinari, H. Garcia, N-doped graphene derived from biomass as a visible-light photocatalyst for hydrogen generation from water/methanol mixtures, *Chem. Eur. J.* 20 (2014) 187–194.
- [43] P.V. Kumar, M. Bernardi, J.C. Grossman, The impact of functionalization on the stability, work function, and photoluminescence of reduced graphene oxide, *ACS Nano* 7 (2013) 1638–1645.
- [44] S. Bai, C. Wang, M. Deng, M. Gong, Y. Bai, J. Jiang, Y. Xiong, Surface polarization matters: enhancing the hydrogen-evolution reaction by shrinking Pt shells in Pt–Pd–graphene stack structures, *Angew. Chem. Int. Ed.* 53 (2014) 12120–12124.
- [45] S. Bai, L. Yang, C. Wang, Y. Lin, J. Lu, J. Jiang, Y. Xiong, Boosting photocatalytic water splitting: interfacial charge polarization in atomically controlled core-shell co-catalyst, *Angew. Chem. Int. Ed.* 54 (2015) 14810–14814.
- [46] Z. Zhan, L. Zheng, Y. Pan, G. Sun, L. Li, Self-powered, visible-light photodetector based on thermally reduced graphene oxide–ZnO (rGO–ZnO) hybrid nanostructure, *J. Mater. Chem.* 22 (2012) 2589–2595.
- [47] G. Fan, H. Zhu, K. Wang, J. Wei, X. Li, Q. Shu, N. Guo, D. Wu, Graphene/silicon nanowire Schottky junction for enhanced light harvesting, *ACS Appl. Mater. Interfaces* 3 (2011) 721–725.
- [48] C. Kong, S. Min, G. Lu, Robust Pt–Sn alloy decorated graphene nanohybrid cocatalyst for photocatalytic hydrogen evolution, *Chem. Commun.* 50 (2014) 9281–9283.
- [49] S. Min, G. Lu, Dye-sensitized reduced graphene oxide photocatalysts for highly efficient visible-light-driven water reduction, *J. Phys. Chem. C* 115 (2011) 13938–13945.
- [50] S. Zhuang, X. Xu, B. Feng, J. Hu, Y. Pang, G. Zhou, L. Tong, Y. Zhou, Photogenerated carriers transfer in dye-graphene–SnO₂ composites for highly efficient visible-light photocatalysis, *ACS Appl. Mater. Interfaces* 6 (2014) 613–621.
- [51] Q. Zhao, M. Ji, H. Qian, B. Dai, L. Weng, J. Gui, J. Zhang, M. Ouyang, H. Zhu, Controlling structural symmetry of a hybrid nanostructure and its effect on efficient photocatalytic hydrogen evolution, *Adv. Mater.* 26 (2014) 1387–1392.